



# Shock wave confinement-induced plume temperature increase in laser-induced breakdown spectroscopy



Chong Li<sup>a</sup>, Jianmei Wang<sup>b</sup>, Xinwei Wang<sup>a,c,\*</sup>

<sup>a</sup> 2010 Black Engineering Building, Department of Mechanical Engineering, Iowa State University, Ames, IA 50011, USA

<sup>b</sup> Department of Energy and Power Engineering, Wuhan University, Wuhan 430072, PR China

<sup>c</sup> School of Urban Development and Environmental Engineering, Shanghai Second Polytechnic University, Shanghai 201209, PR China

## ARTICLE INFO

### Article history:

Received 20 March 2014

Received in revised form 30 May 2014

Accepted 1 June 2014

Available online 27 September 2014

Communicated by R. Wu

### Keywords:

Laser-induced breakdown spectroscopy

Shock wave spatial confinement

Molecular dynamics

Atomic collision/friction

Temperature and lifetime increase

## ABSTRACT

Spatial confinement is found effective in improving the sensitivity of laser-induced breakdown spectroscopy (LIBS). This work reports on the physics of shock wave spatial confinement via atomistic modeling. Reflection-induced atomic collision/friction near the wall reduces the shock wave velocity close to zero and remarkably increases the local temperature ( $\sim 218$  K) and pressure. As a result, the reflected ambient gas expands quickly toward the plume and compresses it. The temperature of the plume goes up significantly in the compression process: from 89 to 132 K. The lifetime of the plume is also boosted dramatically, from 480 ps to  $\sim 1800$  ps.

© 2014 Elsevier B.V. All rights reserved.

## 1. Introduction

Laser-induced breakdown spectroscopy (LIBS) is a technique developed for element analysis with a laser serving as the excitation source. The wavelength of the electromagnetic irradiation from the excited plasma at high temperatures is analyzed selectively for the presence of analytes and the intensity is proportional to their content concentration in the sample [1–4]. In the past decades, LIBS has been developed into a mature technology and is widely used in multi-component analysis of element composition [5,6], cultural heritage in-situ investigation [7,8], steel manufacturing industry [2,9], environmental monitoring [10] etc.

All of the analyses are carried out based on the frequencies of the emitting light from the elements when it is excited to a sufficiently high temperature. Several factors, such as the plasma excitation temperature, the light collection window and the line strength of the viewed transition affect the sensitivity and accuracy of LIBS. A lot of works have been devoted to improving this technique. All the experimental components in LIBS can be made to be miniature and portable. And a large number of works are carried out to make this technique reliable and rugged in the standoff and

in-situ analysis [11–14]. Dual pulse LIBS was proposed as a way to overcome the shortcoming of poor sensitivity of the conventional single pulse LIBS by increasing the efficiency of the production of analyte atoms in the excited state [15–18]. At the same time, the combinations of lasers of different wavelengths, pulse sequence and pulse width were investigated for the optimal performance in LIBS [19–21]. Long nanosecond pulses were discovered to be more favorable for the LIBS application due to the relatively slow heating of the plasma, causing a larger and less-dense plume and therefore fairly intense and less broadened emission lines [22,23].

Recently, spatial confinement has captured a lot of attention from researchers. It was found effective in increasing the plasma shock wave pressure [24]. Plasma temperature increase and enhanced emission intensity were also observed [25–28]. Different spatial confinement shapes have been studied in Lu's group, which include a pair of parallel walls [25], a pipe [26], and a hemispherical cavity [27]. A temperature rise as high as 3600 K was reported by their group in the Mn element analysis excited by the KrF excimer laser with the sample trapped in a hemispherical cap. The compression of the plasma by the reflected shock wave was found to account for the increase of the plasma temperature. Consequently, it leads to great sensitivity improvement of LIBS.

In spite of the interesting spatial confinement phenomenon and the significant temperature and intensity enhancement, little work has been done to unveil the underlying physical mechanism in the sensitivity enhancement. Molecular dynamic (MD) simulation is employed in this work and a potential wall boundary condition

\* Corresponding author at: 2010 Black Engineering Building, Department of Mechanical Engineering, Iowa State University, Ames, IA 50011, USA. Tel.: +1 515 294 2085; fax: +1 515 294 3261.

E-mail address: [xwang3@iastate.edu](mailto:xwang3@iastate.edu) (X. Wang).

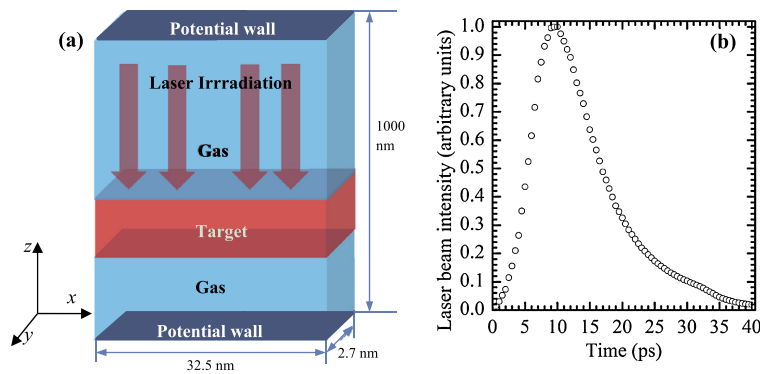


**Fig. 1.** (a) Atomic configuration of the model for the case with spatial confinement. The entire simulation box measures  $32.5 \times 2.7 \times 1000 \text{ nm}^3$  ( $x \times y \times z$ ). The target measures  $32.5 \times 2.7 \times 108.3 \text{ nm}^3$  ( $x \times y \times z$ ). The gap between the bottom of the target and the bottom of the simulation box is 271 nm. Laser energy propagates in the negative  $z$  direction. For the confinement case, the upper and lower boundaries along the  $z$  direction are in wall/LJ93 potential. The other four boundaries are periodic. For the free-space case, the simulation box size is  $32.5 \times 2.7 \times 3627 \text{ nm}^3$ . The target size and location remains the same as the spatial confinement case. But the six boundaries are in periodic boundary condition. (b) Laser profile. The FWHM of the pulse is 11.5 ps, and the peak is located at 9 ps. Laser fluence in this work is  $5 \text{ J/m}^2$ .

is adopted to simulate the wall confinement. A comparison of the confinement case (with potential walls) and free-space case (without potential walls) is made, in an attempt to uncover the energy conversion process and the enhancement physics.

## 2. Methodologies of simulation

The argon crystal is in the simple face-centered cubic structure and the atom–atom interactions can be easily described by the Lennard–Jones (12–6) potential. A lot of works in our group [29–31] have proven the simplicity of modeling and computation as well as the validity of exploring the physical mechanisms in laser–material interaction. Given the advantage of argon in large-scale and long-time computation without losing the generality of conclusion, it is chosen as the material for investigation in this work. The LJ potential well depth  $\varepsilon$  is  $1.653 \times 10^{-21} \text{ J}$  and equilibrium separation parameter  $\sigma$  is 3.406 Å. And the cut-off distance is set to  $2.5\sigma$ . A large domain size and a long laser pulse require more time for computation. To achieve an efficient computation, a picosecond laser pulse and a nanometer size domain are adopted. For the convenience of comparison, simulations of the cases with potential walls and without potential walls are conducted. The main difference lies in the boundary condition settings. The spatial confinement is accomplished by the wall boundary condition while the free space condition is achieved by the periodic boundary condition. Fig. 1 shows the model size of the case with potential walls in this work. The whole simulation box measures  $32.5 \times 2.7 \times 1000 \text{ nm}^3$  ( $x \times y \times z$ ) and the case with free space has a box size of  $32.5 \times 2.7 \times 3627 \text{ nm}^3$  ( $x \times y \times z$ ). The target size is  $32.5 \times 2.7 \times 108.3 \text{ nm}^3$  for both cases. The gap between the bottom of the target and the bottom of the simulation box is 271 nm. The total atom number is 264 660 for the confinement case and 337 500 for the free-space case.

The case with potential walls is employed to investigate the spatial confinement effect. A wall potential (wall/LJ93) is implemented in the upper and lower boundaries along the  $z$  direction. The other four boundaries are periodic. The strength factor  $\varepsilon$  for wall–atom interaction is  $1.653 \times 10^{-21} \text{ J}$  and the size factor  $\sigma$  is 3.615 Å in this work. 8.515 Å is chosen as the cutoff distance for the wall boundary. 5 fs is chosen as the time step for the simulation. For the free-space case, periodic boundary conditions are applied in all six boundaries. More details concerning the setup of the models can be seen in our previous work [30,31].

The LAMMPS package [32] is employed in this work. The whole simulation system is thermostated as a canonical (NVT) ensemble at the temperature  $T = 50 \text{ K}$  for 1 ns. Afterward, the system is run as a microcanonical (NVE) ensemble for 500 ps to remove the

disturbance in the temperature adjustment. Thermal equilibrium is reached after the NVE computation and the ambient pressure is 0.23 MPa in equilibrium for both cases.

The laser irradiation happens right after NVE. The full width at half maximum (FWHM) of the incident laser beam intensity distribution is 11.5 ps and the peak is at 9 ps as shown in Fig. 1(b). The laser fluence is  $5 \text{ J/m}^2$  and the pulse duration is 40 ps.

To avoid the downward movement resulting from the laser shock wave and the expected disturbance of the reflected stress wave, a special treatment is applied to the bottom (of size  $\Delta z = 1 \text{ nm}$ ) of the target to absorb the stress wave resulting from the laser irradiation. An external force is added to a specified bottom layer which is approximately  $10 \text{ \AA}$  thick. The force is used to eliminate the stress-induced momentum. The theory and the details of implementation can be seen in our previous work [30,31,33] and the work by Zhigilei [34].

The laser energy propagates in the negative  $z$  direction. The laser energy is absorbed by the target volumetrically and the absorption obeys the Beer–Lambert law. To accomplish this, the target is divided into bins with a thickness of  $\Delta z = 1 \text{ nm}$ . The energy decays exponentially every time step when it passes a layer. The energy absorption is related to the absorption depth (it is 5 nm in this work) and the local material density. The velocity of each atom is rescaled at every time step and the rescaling factor is applied to the three directions in the same manner. In this way, the absorbed energy is converted to thermal energy of the atoms. Details of laser energy absorption and velocity rescaling can be seen in our previous work [30,31].

## 3. Results and discussion

### 3.1. Shock wave confinement and temperature enhancement: general pictures

Two cases: (1)  $E = 5 \text{ J/m}^2$ ,  $\tau = 5 \text{ nm}$ , with spatial confinement and (2)  $E = 5 \text{ J/m}^2$ ,  $\tau = 5 \text{ nm}$  with free space are explored and discussed. The shock wave and plume evolution against time for the case with periodic boundary conditions (free space) has been investigated before. Details can be seen in our previous work [30, 31].

Fig. 2 is a series of snapshots at different times of the case with confinement. The target ablates at first because the laser fluence is above the ablation threshold for argon. The explosive plume then moves upward and pushes the ambient gas (red in the figure) to move forward at a supersonic speed. At  $t = 80 \text{ ps}$ , the shock wave is still in the beginning stage of formation. When it comes to  $t = 400 \text{ ps}$  and  $t = 720 \text{ ps}$ , the shock wave front and plume are split. Interestingly, the ablated atoms are not moving forward with

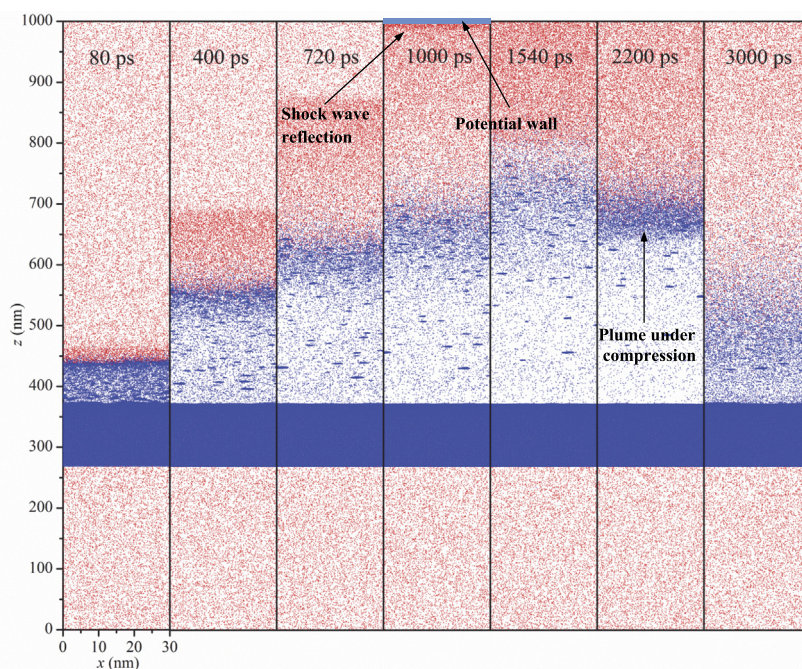


**Fig. 2.** Snapshots of the spatial confinement case. The reflection happens around  $t = 1000$  ps as marked in the figure. Snapshots from  $t = 80$  ps to  $t = 720$  ps are the ones before the reflection and the ambient gas is compressed. Snapshot from  $t = 1540$  ps to  $t = 3000$  ps are after the reflection and the plume is compressed. Before the reflection, the shock wave depth is increasing with time while the plume density is decreasing. After the reflection, the plume is compressed and the plume density increases with time.

the same speed and the plume is separating from each other because of the velocity difference. The density of the plume front is higher than the bottom part since the relatively fast part of plume is constrained by the ambient gas. And this is similar to the shock wave. Considering that the whole simulation box is 1000 nm along the  $z$  direction and the top surface is a potential wall, reflection of the shock wave is expected to occur. Our simulation results show that the shock wave front is reflected at around  $t = 1000$  ps after the laser irradiation.

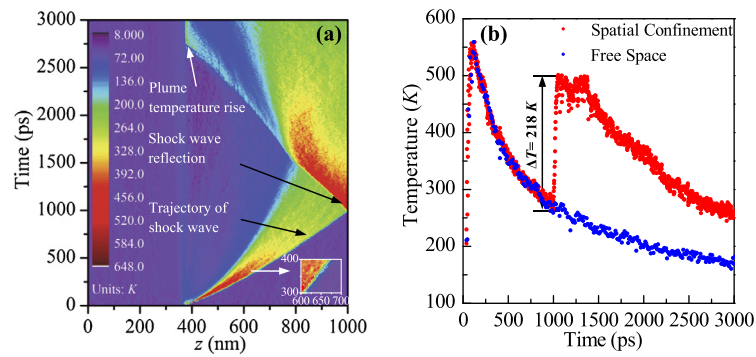
The ambient gas is much denser near the potential wall at  $t = 1000$  ps which is the same time that the reflection occurs as in Fig. 2. Interestingly, the ambient gas is not observed to be reflected immediately at a high speed. Instead, the plume continues to move forward by the comparison of the plots of  $t = 1000$  ps and  $t = 1540$  ps. From the start of the ablation to the moment the shock wave reaches the upper potential wall, the front of the plume becomes less and less dense. While from  $t = 1540$  ps to  $t = 3000$  ps, the plume front is becoming denser and denser, which indicates the plume is under compression from the reflected shock wave. The plume reaches the longest depth at  $t = 1540$  ps in Fig. 2. Along with the compression process, the plume depth is decreasing and finally at  $t = 3000$  ps, the plume and ambient gas have penetrated into each other and the interface of the plume and ambient gas is less distinguishable.

Fig. 3(a) is the temperature contour of the whole simulation system. At the beginning of the material ablation, the ejected plume is at high temperature (above 500 K). Because of the interaction of the plume and the ambient gas, a high temperature shock wave is generated. At the same time, the velocity difference results in the separation of the ejected clusters. The upper part of the plume is at a slightly higher temperature. A closer look at the temperature distribution in the shock wave, as the inset in Fig. 3, reveals that the temperature at first increases to a high value and then drops down along the negative  $z$  direction. The physical front of the shock wave is not at the highest temperature. For the convenience of defining the shock wave front, we assume the layer at the highest temperature in the shock wave region is the shock

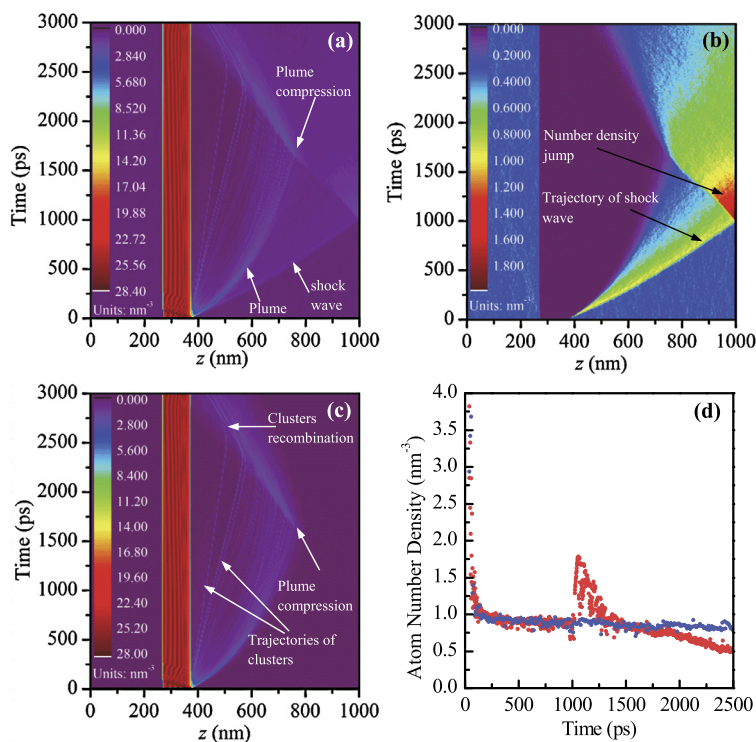
wave front in this work. It is well documented that the shock wave fronts are usually characterized by discontinuities in density and pressure. In the past we have confirmed that in laser-material interaction the highest temperature-defined shock wave front indeed is consistent with that defined by density and pressure discontinuities. For a normal shockwave, temperature, pressure and density all experience discontinuities across the shockwave front. Caution should be exercised on using temperature to define the shock wave front when the shockwave front is not normal to the local propagation front (oblique shock wave).

Fig. 3(b) shows the temperature evolution of the shock wave front against time. In the beginning stage of shock wave formation, a sharp temperature rise occurs. Then the temperature of the shock wave is observed to drop continuously. The data for the case with spatial confinement and the case with free space agree well with each other before the shock wave reaches  $z = 1000$  nm. However, right after the shock wave reaches the wall, the shock wave front temperature jumps from 277 K to 495 K as shown in Fig. 3(b) for the case with confinement. The high temperature remains at around 495 K for 330 ps from 1050 ps to 1380 ps when the plume continues to compress the shock wave. Then the temperature of the shock wave begins to decrease smoothly. There is no temperature rise for the shock wave front of the free-space case after its formation and its temperature drops down smoothly.

When the plume continues to compress the shock wave after  $t = 1000$  ps, the pressure of the upper ambient gas increases and the plume density in the lower part decreases. This also means the pressure difference between the plume and shock wave is becoming larger. Finally, this big pressure difference results in the backward movement of the ambient gas which pushes the plume down, as shown from  $t = 1540$  ps to 3000 ps in Fig. 2. Congruently, in Fig. 3(a), the plume temperature rise is observed after  $t = 1500$  ps which is noticeable around  $t = 2700$  ps. The plume temperature rise in the final stage is of great significance for the sensitivity improvement in LIBS since the temperature rise will elongate the radiation lifetime and increase the signal intensity.



**Fig. 3.** (a) Spatiotemporal contour of temperature. There is a temperature jump of ambient gas right after the reflection at  $t = 1000$  ps. The temperature rise of the plume is also observed when it is compressed by the ambient gas after  $t = 1500$  ps. This temperature rise reaches a very substantial level at about 2700 ps as indicated in the figure. The inset shows that the temperature of the shock wave is not the highest in the physical shock wave front. Instead, the temperature of the shock wave will at first increase to a high value and then decreases smoothly along the negative  $z$  direction. (b) Shock wave front temperature comparison for the cases with spatial confinement and the case with free space. Before  $t = 1000$  ps, the data of the cases with confinement and with free space agree with each other very well. After  $t = 1000$  ps, the temperature of the free-space case drops down smoothly. However, for the case with wall-confinement, a temperature rise of about 218 K is observed.



**Fig. 4.** Number Density contour. (a) Total atom number density which includes both the target atom and the gas atom. The trajectories of the shock wave and the ejected clusters are easily distinguishable. The plume and shock wave split from each other right after the ablation. The shock wave reflection happens at  $t = 1000$  ps. The moving-back gas starts to compress the plume at  $t = 1500$  ps. (b) Ambient gas atom number density. A density jump is observed after the reflection at  $t = 1000$  ps. (c) Target atom number density. The trajectories of the clusters are marked out. After the shock wave is reflected, a lot of clusters combine with each other under the compression of ambient gas. (d) Comparison of the shock wave front atom number density for the case with spatial confinement and free-space case. There is a sudden rise of atom number density right at the moment of reflection. (For interpretation of the references to color in this figure legend, the reader is referred to the web version of this article.)

### 3.2. Shock wave confinement and reflection: physics behind the temperature enhancement

In Fig. 3 we observed a clear temperature rise of the shock wave front after reflection, and a later-on temperature rise of the plume. In this section, we intend to study various aspects of the shock wave and plume, in anticipation to uncover the physics behind the temperature rise. First, we study the mass distribution: atom number density, to gain a fundamental understanding of shock wave confinement and the following compression of the plume by the reflected shock wave. Fig. 4(a)–(c) is the number density contour, which includes the total number density contour, the gas atom density and target atom density contour. The move-

ment of the ejected clusters and the shock wave is quite distinct as marked in Fig. 4(b) and (c).

The shock wave is generated as a result of the compression of the ambient gas by the ejected plume. The plume and the shock wave are observed to split from each other right after the ablation. Because of the velocity difference between them, the gap between the plume and the shock wave grows with time before reflection as shown in Fig. 4(a). Similar to the temperature distribution, the density is not highest at the interface between the shock wave and ambient gas. It increases to a high value and then drops quickly toward the ambient gas. The results show the shock wave front defined using the highest temperature always has the highest density in the shock wave. Right after reflection, there is a number density

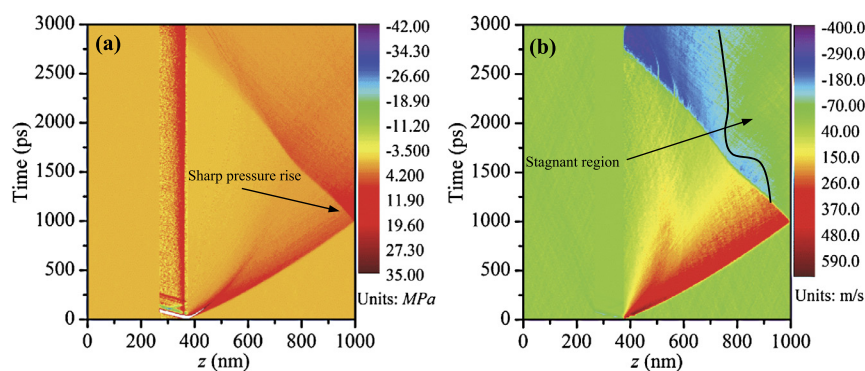


**Fig. 5.** (a) Pressure contour of the whole simulation system. A large compressive stress occurs in the solid at the beginning of laser ablation. With the split of the plume and shock wave, the pressure drops down smoothly. However, at approximately  $t = 1000$  ps, another big pressure occurs in the shock wave due to the reflection and confinement. (b) Velocity contour. The ejected plume has a high velocity. The interaction of the ambient gas and the plume results in the dissipation of the velocity. The plume and the shock wave slow down smoothly before the reflection. The reflection by the potential wall results in a sudden drop of the velocity of the shock wave. Then the ambient gas accelerates to move towards the plume due to the big pressure difference. The ambient gas starts to compress the plume at around  $t = 1500$  ps and the reflected-shock wave stops accelerating at that moment. At the same time, the plume starts to accelerate to move back toward the target surface due to the compression by the reflected ambient gas.

jump due to the continuous compression of the shock wave. This is clearly marked in Fig. 4(b) (the red region close to the wall). After that, the atom number density of the shock wave decreases continuously.

As shown in Fig. 4(c), the ambient gas starts to suppress the plume at approximately  $t = 1500$  ps, causing some of the clusters in the plume to re-combine. An increase of the number density of the plume is observed. Fig. 4(d) shows the comparison of the atom number density of the shock wave front for the case with confinement and free space. The potential wall results in an atom number density increase of almost 2 times in the shock wave front. At the end of the simulation, a small portion of the ambient gas penetrates into the plume. This can also be clearly seen in Fig. 2 at 3000 ps. The shock wave front atom number density is lower than that without spatial confinement from  $t = 1700$  ps due to the continuous relaxation of the reflected-shock wave's pressure.

Fig. 5(a) is the pressure contour of the system. The stress wave in the solid is very clear. For the detailed analysis and discussion of the stress wave in the solid, please refer to our previous work [31,35]. The ablated material in high speed leads to the sharp rise of the ambient gas pressure. Due to the interaction of the shock wave and the ambient gas, the pressure of the shock wave experiences continuous decay before the reflection. However, it is always higher than the plume part and non-shock wave region in the ambient gas. Right after the reflection, a sudden pressure rise is observed around the time  $t = 1000$  ps. Refer to Fig. 2, this is the moment when the shock wave reaches the potential wall and is reflected. Dunbar et al. discovered that the pressure of the shock wave front could increase as many as 11 times in their spatial confinement experiment [24]. Shortly after that, the shock wave pressure decreases as a result of its backward movement and the pressure drops just like the number density. During this backward motion, the pressure of the shock wave is larger than the pressure in the plume region. This is the driving force of the backward movement of the shock wave. At the end of the simulation, the difference in the pressure is blurred and the ambient gas and plume mix with each other. In summary, it is clear that right after the reflection, the shock wave front's pressure is increased dramatically, much higher than the plume's pressure. This pressure difference causes the ambient gas to move back toward the target and the compression of the plume. To have a clearer understanding of this movement reversal process we plot the velocity contour shown in Fig. 5(b).

We clearly see a velocity rise after the ablation and the plume and shock wave move in at different velocities. This finally results

in the separation of the plume and shock wave. The atom collision brings the velocity of the ambient gas adjacent to the wall area close to 0 when the shock wave arrives at the potential wall and is reflected back. A large part of the kinetic energy of the shock wave is converted to thermal energy due to the collision. Therefore, a sudden temperature rise occurs. The pressure also increases abruptly at this moment as shown in Fig. 5(a). Then, the remaining part of shock wave that is moving forward collides with the atoms in the high pressure region and the velocity is absorbed quickly. Consequently, the stagnant region marked in Fig. 5(b) increases with time.

After reflection by the wall, the velocity of the shock wave increases with time due to the fact that its pressure is higher than that in the plume, as illustrated in Fig. 5(a). This is due to the phenomenon that the compressed shock wave front accumulates in the near-wall region, leading to a very high local pressure. Interestingly, after the reflection, only the interface of the ambient gas and the plume possess a high velocity. The other parts are almost stagnant as marked in Fig. 5(b). The velocity of the upper ambient gas in the region  $z > 740$  nm is around zero since  $t = 1900$  ps. This means their kinetic energy is almost completely converted into thermal energy. Fig. 3(a) shows this stagnant region has a stable and high temperature. When the plume is under compression from the reflected shock wave, its velocity starts to decrease to zero. Then it moves toward the target surface. The highest velocity of the plume occurs at the end of the simulation. The pressure of the plume also increases because of the compression by the shock wave. Similar to the temperature rise at the moment of reflection of the shock wave, the shock wave's collision with the plume and with the ambient gas contributes to the temperature increase of the plume.

### 3.3. Temperature and lifetime of plume

In LIBS, the critical factors determining the signal intensity and probing sensitivity are the temperature and lifetime of the plume. In this section, these two factors are studied in detail under the shock wave confinement. Fig. 6(a) is the comparison of the velocity of the shock wave front for the case with confinement and the case with free space. A sharp jump in the velocity of the shock wave front occurs when the shock wave forms. The reflection occurs at around  $t = 1000$  ps. Before  $t = 1000$  ps, the two lines are almost the same. For the free-space case, the velocity decreases smoothly with time. However, in the spatial confinement case, the velocity drops from 311 m/s to 0 suddenly at  $t = 1000$  ps due

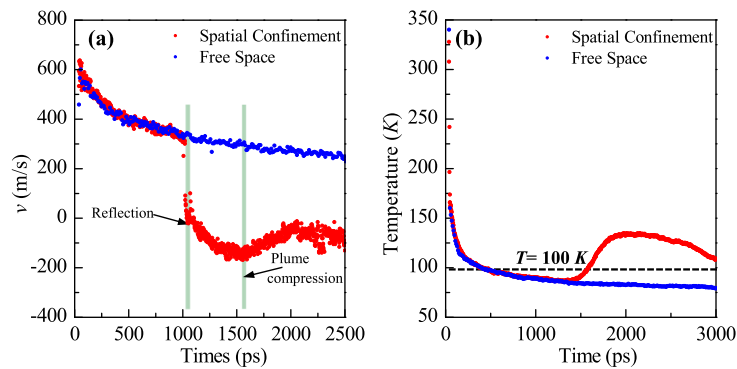


**Fig. 6.** (a) Velocity comparison for the cases with and without confinement. Before the reflection ( $t = 1000$  ps), the results of the two cases agree well with each other. The reflection results in a sudden drop of velocity (from 324 m/s to 0). The reflected-shock wave accelerates to move back towards the plume and then slows down. (b) Plume average temperature comparison. Only the plume above  $z \leq 400$  nm is counted in this work for temperature calculation. For the confinement case, the temperature drops down at first due to the interaction of the plume and the ambient gas. Part of the energy is transferred from the plume to the ambient gas. The plume is compressed by the ambient gas from  $t = 1500$  ps. The plume temperature is observed to increase at this very moment. After  $t = 2500$  ps, part of the plume is pushed to the region below  $z = 400$  nm. The plume temperature decreases again. However, for the free-space case, the temperature decreases smoothly with time. Meanwhile, the time for the plume to stay above 100 K has been increased from 480 ps to 1800 ps because of the confinement.

to wall reflection. Then the shock wave front moves toward the plume with an increasing velocity. This is because the accumulated shockwave front in the near-wall region induces a very high local pressure. This high pressure pushes the ambient gas to move toward the target surface region, where the local pressure is much lower. Around  $t = 1500$  ps, the velocity begins to decrease and is approximately zero after  $t = 2000$  ps. The decrease in velocity starting at 1500 ps results from the collision of the backward-moving shock wave and the forward-moving plume. Starting from this moment, the backward-moving shock wave is in contact with the plume, and pushes them backward. Therefore, the shock wave front velocity begins to decrease. The kinetic energy of the ambient gas is converted to thermal energy. A large part of the energy is transferred to the plume through the compression and collision afterwards.

Fig. 6(b) is the average temperature of the plume. To calculate the temperature, we choose the target atoms above  $z = 400$  nm, which moderately represent the plume in the physical process. The laser burst results in a sudden rise of the plume temperature. After that, the energy of the plume is transferred to the ambient gas and the temperature drop is observed. At the same time the plume and shock wave front are separating with each other and the gap is increasing with time, which means the interaction between the plume and shock wave is weakening. As a result, the rate of the temperature drop is decreasing with time as shown in Fig. 6(b). Around  $t = 1500$  ps, there is a sharp temperature rise from 89 K to 132 K for the spatial-confinement case. This occurs at the same moment when the reflected-shock wave begins to compress the plume. The compression of the plume is the reason for the temperature rise. In the experiment, a temperature rise of the plasma as high as 3600 K (hemispherical cavity) and 1000 K (cylinder confinement) has been reported in Lu's group [26,27]. After  $t = 2500$  ps, the plume temperature begins to decrease, because only the plume that is above  $z = 400$  nm is considered in the temperature calculation and part of the plume is pushed back below that region after  $t = 2500$  ps. It is a little hard to define the life time of the plume that can be useful during LIBS in our case since we do not know exactly above what temperature the plume will emit useful radiation that could be detected. The boiling point of argon is 87.35 K. If we take a value of 100 K as the criterion above which the plume is assumed to be able to emit useful radiation, some first-order life time analysis can be conducted here. As shown in Fig. 6(b), the time for the temperature above 100 K in the case with confinement is more than 1800 ps. In contrast, the time above 100 K in the free-space case is only 480 ps. The life-

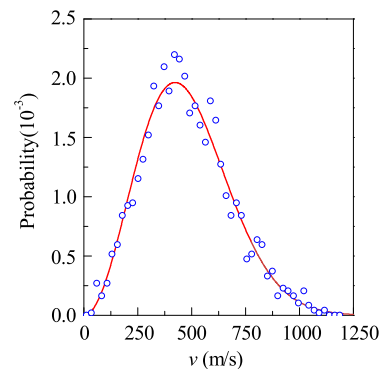


**Fig. 7.** Comparison of the velocity distribution of atoms ranging from  $z = 975$  nm to  $z = 985$  nm at  $t = 1200$  ps with Maxwellian velocity distribution. The solid line is the Maxwellian velocity distribution at  $T = 430$  K which is the average temperature of the atoms in the selected region. The hollow dots are the velocity distribution of atoms in MD simulation.

time of the plume is significantly elongated by 1320 ps which is very beneficial for more sensitive detection in LIBS.

Although it is apparent that both the ambient gas and the plume experience a temperature rise, it is still possible that the average temperature in the contour maybe misleading. The average velocity of the ambient gas is around zero after the reflection. [Fig. 5(b)] There is a possibility that the reflected atoms and the forward-moving atoms have the same velocity but in opposite directions. Under such a scenario, the average velocity is still zero, but a lot of the movement is macro-scale translational movement, and cannot be used for temperature calculation. To confirm that the temperature in our case is the real temperature, the velocity distribution comparison with the velocity in the thermal equilibrium state (Maxwellian distribution) is given as Fig. 7. The atoms ranging from  $z = 975$  nm to  $z = 985$  nm are chosen as the region for the analysis here. The average temperature in that region at  $t = 1200$  ps is 430 K. The actual velocity data fits the Maxwell curve of velocity distribution in 430 K as in Fig. 7. This proves the validity of our temperature evaluations.

#### 4. Conclusions

In this work, MD simulations were conducted to investigate the spatial confinement effect on shock wave and the resulting boost in plume temperature and lifetime. The temperature, pressure and number density of the shock wave were observed to increase dramatically immediately after the reflection from the wall.

The reflected shock wave and the forward-moving shock wave had a strong collision, and such an atomic collision/friction makes the velocity of the shock wave decreases to almost zero after reflection. This means a large part of the kinetic energy is converted to the thermal energy of the shock wave. A temperature rise as high as 218 K was observed for the shock wave front after the wall reflection. The big difference of the pressure between the plume and ambient gas after the reflection caused the ambient gas to move back towards the plume. Finally, the plume was compressed by the reflected shock wave. In the compression process, the ejected clusters recombined with each other. The downward velocity of the plume increased dramatically. More importantly, the temperature of the plume is enhanced dramatically from 89 K to 132 K. Also this high temperature was maintained for quite a long time. This explains the sensitivity enhancement in the spatial confinement of LIBS. If we took 100 K as the criterion for plume radiation sensing in our modeling, the lifetime of the plume was increased from 480 ps (free space case) to more than 1800 ps. This could further improve the sensitivity of LIBS via spatial confinement.

### Acknowledgements

Support of this work by the National Science Foundation (No. CMMI-1029072 and No. CMMI-1200397) is gratefully acknowledged. X.W. thanks the partial support of “Eastern Scholar” program of Shanghai, China.

### References

- [1] F.J. Fortes, J. Moros, P. Lucena, L.M. Cabalín, J.J. Laserna, Laser-induced breakdown spectroscopy, *Anal. Chem.* 85 (2012) 640–669.
- [2] R. Noll, H. Bette, A. Brysch, M. Kraushaar, I. Mönch, L. Peter, V. Sturm, Laser-induced breakdown spectrometry – applications for production control and quality assurance in the steel industry, *Spectrochim. Acta, Part B, At. Spectrosc.* 56 (2001) 637–649.
- [3] D.W. Hahn, N. Omenetto, Laser-induced breakdown spectroscopy (LIBS). Part II: review of instrumental and methodological approaches to material analysis and applications to different fields, *Appl. Spectrosc.* 66 (2012) 347–419.
- [4] L.J. Radziemski, From LASER to LIBS, the path of technology development, *Spectrochim. Acta, Part B, At. Spectrosc.* 57 (2002) 1109–1113.
- [5] J.D. Pedarnig, P. Kolmhofer, N. Huber, B. Praher, J. Heitz, R. Rössler, Element analysis of complex materials by calibration-free laser-induced breakdown spectroscopy, *Appl. Phys. A* 112 (2012) 105–111.
- [6] I.B. Gornushkin, B.W. Smith, H. Nasajpour, J.D. Winefordner, Identification of solid materials by correlation analysis using a microscopic laser-induced plasma spectrometer, *Anal. Chem.* 71 (1999) 5157–5164.
- [7] R. Gaudioso, M. Dell’Aglia, O.D. Pascale, G.S. Senesi, A.D. Giacomo, Laser induced breakdown spectroscopy for elemental analysis in environmental, cultural heritage and space applications: a review of methods and results, *Sensors* 10 (2010) 7434–7468.
- [8] S. Georgiou, D. Anglos, C. Fotakis, Photons in the service of our past: lasers in the preservation of cultural heritage, *Contemp. Phys.* 49 (2008) 1–27.
- [9] V. Sturm, J. Vrenegor, R. Noll, M. Hemmerlin, Bulk analysis of steel samples with surface scale layers by enhanced laser ablation and LIBS analysis of C, P, S, Al, Cr, Cu, Mn and Mo, *J. Anal. At. Spectrom.* 19 (2004) 451–456.
- [10] O.T. Butler, W.R.L. Cairns, J.M. Cook, C.M. Davidson, Atomic spectrometry update. Environmental analysis, *J. Anal. At. Spectrom.* 27 (2012) 187–221.
- [11] R.S. Harmon, F.C. DeLucia, C.E. McManus, N.J. McMillan, T.F. Jenkins, M.E. Walsh, A. Miziolek, Laser-induced breakdown spectroscopy – an emerging chemical sensor technology for real-time field-portable, geochemical, mineralogical, and environmental applications, *Appl. Geochem.* 21 (2006) 730–747.
- [12] C.G. Brown, R. Bernath, M. Fisher, M.C. Richardson, M. Sigman, R.A. Walters, A. Miziolek, H. Bereket, L.E. Johnson, Remote femtosecond laser induced breakdown spectroscopy (LIBS) in a standoff detection regime, *Proc. SPIE* 6219 (2006) 62190B-1–62190B-7.
- [13] J. Gruber, J. Heitz, H. Strasser, D. Bäuerle, N. Ramaseder, Rapid in-situ analysis of liquid steel by laser-induced breakdown spectroscopy, *Spectrochim. Acta, Part B, At. Spectrosc.* 56 (2001) 685–693.
- [14] O. Samek, D.C.S. Beddows, J. Kaiser, S.V. Kukhlevsky, M. Liška, H.H. Telle, et al., Application of laser-induced breakdown spectroscopy to in situ analysis of liquid samples, *Opt. Eng.* 39 (2000) 2248–2262.
- [15] J. Scaffidi, S.M. Angel, D.A. Cremers, Emission enhancement mechanisms in dual-pulse LIBS, *Anal. Chem.* 78 (2006) 24–32.
- [16] L. St-Onge, V. Detalle, M. Sabsabi, Enhanced laser-induced breakdown spectroscopy using the combination of fourth-harmonic and fundamental Nd:YAG laser pulses, *Spectrochim. Acta, Part B, At. Spectrosc.* 57 (2002) 121–135.
- [17] R.W. Coons, S.S. Harilal, S.M. Hassan, A. Hassanein, The importance of longer wavelength reheating in dual-pulse laser-induced breakdown spectroscopy, *Appl. Phys. B* 107 (2012) 873–880.
- [18] V.I. Babushok, F.C. DeLucia Jr., J.L. Gottfried, C.A. Munson, A.W. Miziolek, Laser induced breakdown spectroscopy signal enhancement, *Spectrochim. Acta, Part B, At. Spectrosc.* 61 (2006) 999–1014.
- [19] J. Chen, Z. Chen, J. Sun, X. Li, Z. Deng, Y. Wang, Effects of laser pulse sequence on laser-induced soil plasma emission, *Appl. Opt.* 51 (2012) 8141–8146.
- [20] G. Abdellatif, H. Imam, A study of the laser plasma parameters at different laser wavelengths, *Spectrochim. Acta, Part B, At. Spectrosc.* 57 (2002) 1155–1165.
- [21] F. Anabitarte, A. Cobo, J.M. Lopez-Higuera, Laser-induced breakdown spectroscopy: fundamentals, applications, and challenges, *ISRN Spectrosc.* 2012 (2012) 1–12.
- [22] A. Elhassan, A. Giakoumaki, D. Anglos, G.M. Ingo, L. Robbiola, M.A. Harith, Nanosecond and femtosecond laser induced breakdown spectroscopic analysis of bronze alloys, *Spectrochim. Acta, Part B, At. Spectrosc.* 63 (2008) 504–511.
- [23] N. Agnes, H.-Y. Tao, Z.-Q. Hao, C.-K. Sun, X. Gao, J.-Q. Lin, A comparison of single shot nanosecond and femtosecond polarization-resolved laser-induced breakdown spectroscopy of Al, *Chin. Phys. B* 22 (2013) 014209.
- [24] T. Dunbar, B. Maynard, D.A. Thomas, M.D.M. Peri, I. Varghese, C. Cetinkaya, Pressure amplification of laser induced plasma shockwaves with shock tubes for nanoparticle removal, *J. Adhes. Sci. Technol.* 21 (2007) 67–80.
- [25] X.K. Shen, J. Sun, H. Ling, Y.F. Lu, Spatial confinement effects in laser-induced breakdown spectroscopy, *Appl. Phys. Lett.* 91 (2007) 081501.
- [26] X.K. Shen, J. Sun, H. Ling, Y.F. Lu, Spectroscopic study of laser-induced Al plasmas with cylindrical confinement, *J. Appl. Phys.* 102 (2007) 093301.
- [27] L.B. Guo, C.M. Li, W. Hu, Y.S. Zhou, B.Y. Zhang, Z.X. Cai, X.Y. Zeng, Y.F. Lu, Plasma confinement by hemispherical cavity in laser-induced breakdown spectroscopy, *Appl. Phys. Lett.* 98 (2011) 131501.
- [28] A.M. Popov, F. Colao, R. Fantoni, Enhancement of LIBS signal by spatially confining the laser-induced plasma, *J. Anal. At. Spectrom.* 24 (2009) 602–604.
- [29] X. Wang, X. Xu, Molecular dynamics simulation of heat transfer and phase change during laser material interaction, *J. Heat Transf.* 124 (2001) 265–274.
- [30] S. Gacek, X. Wang, Dynamics evolution of shock waves in laser–material interaction, *Appl. Phys. A* 94 (2008) 675–690.
- [31] C. Li, J. Zhang, X. Wang, Phase change and stress wave in picosecond laser–material interaction with shock wave formation, *Appl. Phys. A* 112 (2013) 677–687.
- [32] S. Plimpton, Fast parallel algorithms for short-range molecular dynamics, *J. Comput. Phys.* 117 (1995) 1–19.
- [33] L. Zhang, X. Wang, Hybrid atomistic–macroscale modeling of long-time phase change in nanosecond laser–material interaction, *Appl. Surf. Sci.* 255 (2008) 3097–3103.
- [34] B.J.G. Leonid V. Zhigilei, Pressure waves in microscopic simulations of laser ablation, *Mater. Res. Soc. Symp. Proc.* 538 (1999) 491–496.
- [35] X. Wang, X. Xu, Molecular dynamics simulation of thermal and thermomechanical phenomena in picosecond laser material interaction, *Int. J. Heat Mass Transf.* 46 (2003) 45–53.